

## CdS/g-C<sub>3</sub>N<sub>5</sub> for heterogeneous catalytic degradation of hazardous pollutants

T. Cui, K. L. Wan, W. Yan, Y. C. Wei, Y.P. Chen, J. Xu \*

*School of Physics and Electronic Engineering, Jiangsu University, Zhenjiang, China*

CdS, as an important photocatalytic degradation material, exhibits certain limitations. In our study, carbon nitride/cadmium sulfide (C<sub>3</sub>N<sub>5</sub>/CdS) nanocomposites were synthesized via an in-situ method, and the crystalline structure, composition, and morphology of the hybrid samples were evaluated using various techniques. The development of the Z-scheme heterojunction in the C<sub>3</sub>N<sub>5</sub>/CdS composite photocatalyst facilitated more effective separation of photogenerated charges, resulting in higher photocatalytic degradation efficiency. Under visible light irradiation at 425 nm, the composite with a 1:1 ratio exhibited the best degradation performance, achieving degradation rates of 93.8% for methyl orange solution and 96.8% for rhodamine B solution. Additionally, the introduction of C<sub>3</sub>N<sub>5</sub> significantly reduced the photocorrosion of CdS. These experimental results were confirmed by fluorescence analysis, surface photovoltage (SPV) measurements, electrochemical tests, etc.

(Received July 4, 2024; Accepted August 5, 2024)

*Keywords:* N-rich carbon nitride, Cadmium sulfide, Photocatalytic, Degradation, Textile wastewater, Z-type heterojunction

### 1. Introduction

Textile wastewater exhibits a complex composition, with typical pollutants like methyl orange (MO) and methyl blue (MB) characterized by high toxicity, intense coloration, resistance to photodegradation, and thermal stability. Conventional treatment methods, including physical sedimentation, filtration, chemical precipitation, chemical oxidation, and biological processes, are often ineffective in rapidly and economically degrading textile wastewater [1]. The persistent nature of these pollutants demands innovative and effective treatment technologies. The global energy crisis underscores the urgent need for renewable energy sources. Photocatalysis, leveraging solar energy to initiate chemical reactions, stands out as a sustainable solution, offering significant advancements in environmental remediation and energy conversion, including hydrogen production from water splitting [2].

CdS is well-known for its visible light-responsive properties and shows great potential in photocatalytic applications because it can effectively generate charge carriers under sunlight exposure. Its abilities to degrade organic pollutants and produce hydrogen are well-established. However, practical applications are often limited by the rapid recombination of charge carriers and significant photo corrosion issues. To address the inherent challenges of CdS, such as photo corrosion and fast electron-hole pair recombination, various strategies have been developed. These strategies include doping with metals and non-metals, surface modifications, and constructing heterojunctions with complementary semiconductors to improve charge separation and stability [3-4]. These improvements aim to overcome the limitations of CdS, thereby extending its applicability and effectiveness in environmental remediation technologies.

Graphitic carbon nitride (g-C<sub>3</sub>N<sub>5</sub>) as a polymer semiconductor material has proven to be very useful in the area of photocatalysis because it is stable and energy efficient. Especially when it is integrated into the photocatalytic system, its role cannot be ignored, it significantly improves electron-hole separation and visible light absorption. Moreover, combining g-C<sub>3</sub>N<sub>5</sub> with CdS has been shown to effectively mitigate electron-hole recombination issues, thereby enhancing both the stability and efficiency of photocatalytic processes [5]. Although CdS/CN composites have shown

\*Corresponding author: xjing@ujs.edu.cn  
<https://doi.org/10.15251/DJNB.2024.193.1187>

some photocatalytic activity, there is still a large room for improvement in terms of efficiency and selectivity. In the current research, there is still a lack of comprehensive and in-depth understanding of how to optimize the photocatalytic performance of CdS/CN composites through microstructure engineering. This study addresses these gaps by employing in situ synthesis to develop CdS/C<sub>3</sub>N<sub>5</sub> composites, to substantially enhance CdS's photocatalytic degradation efficiency through the synergistic effects of the CdS/C<sub>3</sub>N<sub>5</sub> heterojunction for effective pollutant degradation. The structural and functional properties are assessed by a variety of characterization methods, among which X-ray diffraction (XRD), scanning electron microscopy (SEM), and photoluminescence spectroscopy play a key role in creating an understanding of the microstructure of materials. These analyses underscore the promising potential of these materials to enable significant progress in photocatalytic applications [6].

In this study, a series of novel CdS/C<sub>3</sub>N<sub>5</sub> (CCN) frameworks with various weight ratios (1:8, 1:2, 1:4, 1:1, and 2:1) were fabricated. Under visible light (425 nm), the composites were evaluated for their ability to photodegrade methylene orange and Rhodamine B, demonstrating that integrating CdS with g-C<sub>3</sub>N<sub>5</sub> not only mitigates the rapid reorganization of charge carriers but also improves photocatalytic stability and efficiency. This integration presents a practical solution for environmental remediation.

## **2. Materials and methods**

### **2.1. Materials**

Cadmium nitrate tetrahydrate, sodium sulfide, and 1H-1,2, 4-triazole-5-amine are all of analytical purity, so no further purification is needed. These chemicals have reached high purity standards and are suitable for relevant experimental studies.

### **2.2. Synthesis of C<sub>3</sub>N<sub>5</sub>(CN)**

Thermal polymerization produces graphite carbon nitride (g-C<sub>3</sub>N<sub>5</sub>). First, 5.0 g of aminotriazole was added to the crucible for subsequent experiments, which was then inserted into a muffle furnace. The furnace temperature was gradually increased to 500 °C at a controlled heating rate of 5 °C per minute. After reaching this temperature, the furnace maintained it for 3 hours to promote the polymerization and graphitization of the precursor. The furnace naturally cools to room temperature after heating. The resulting solid was extracted from the crucible and ground into a fine powder, yielding block g-C<sub>3</sub>N<sub>5</sub>, referred to as CN.

### **2.3. Synthesis of CdS/C<sub>3</sub>N<sub>5</sub> composites (CCN)**

A total of four aliquots of cadmium nitrate, each weighing 0.525 g, were dissolved in separate batches of deionized water, each containing 150 mL. Various mass ratios of the C<sub>3</sub>N<sub>5</sub> photocatalyst (25 mg, 50 mg, 100 mg, 200 mg, 400mg) were then added to these solutions and stirred for one hour till they were completely mixed. After that, four aliquots of sodium sulfide were added, each being 0.416g. In 20 ml of deionized water, sodium sulfide is dissolved, and then ultrasonication is applied to the solution to ensure an even distribution of sodium sulfide. The sonicated sodium sulfide solutions were then added dropwise to the continuously stirred Cd(NO<sub>3</sub>)<sub>2</sub>/C<sub>3</sub>N<sub>5</sub> mixtures. Stirring was maintained in the absence of light for an additional two hours, after which the mixtures were allowed to stand undisturbed for 12 hours to facilitate phase separation. Upon separation of the precipitate from the supernatant, the orange-yellow precipitate was isolated via centrifugation and subsequently dried under vacuum. The catalysts obtained were designated as CCNx, where 'x' denotes the mass ratio of C<sub>3</sub>N<sub>5</sub> to CdS. In the absence of C<sub>3</sub>N<sub>5</sub>, pure CdS samples were produced [7,8].

### **2.4. Experimental evaluation of contaminant degradation**

This study initially assessed the photocatalytic degradation capabilities of methyl orange and rhodamine within the CdS/CN reaction system. The experimental setup was such that, the reaction system containing 10 mg of CCN was tested against solutions of methyl orange and rhodamine at a concentration level of 10 mg/L each. Before the experiment, we chose an LED lamp

with a wavelength of 425 nm as the light source. The sample will be exposed to this light source before proceeding to the next steps, CCN was added to 50 mL of methyl orange or rhodamine solution. The adsorption-desorption equilibrium is the final part, you keep it dark and stir it continuously for 30 minutes to make sure that it is well combined. Subsequently, the mixture was subjected to visible light exposure to initiate the process of photocatalytic degradation. Throughout the process, we recorded data at 10-minute intervals to monitor the progress of the reaction, 3 mL samples were extracted and filtered, with the concentrations of methyl orange and rhodamine measured at 463 nm and 554 nm wavelengths, respectively, using a UV-visible spectrophotometer. In addition, The mixture is then exposed to visible light to start the photocatalytic degradation process. Throughout the process, we recorded data at 10-minute intervals to monitor the progress of the reaction.

Besides, to assess the photocatalytic activity of CCN at different initial concentrations of methyl orange, the best-performing CCN ratio was chosen for degradation experiments in solutions with 20 mg/L, 30 mg/L, and 40 mg/L of methyl orange [9]. These experiments were conducted under consistent lighting and stirring conditions to ensure the comparability of the data. Samples were taken every 10 minutes during the illumination, and a UV-visible spectrophotometer working at 463 nm observed methyl orange degradation.

### 3. Results and discussion

#### 3.1. Synthesis and characterization

The solid yellow CN powder was deposited onto CdS photocatalysts through in situ synthesis (Fig. 1). The micro-morphology and structure of CdS, CN, and CCN samples were analyzed using scanning electron microscopy. SEM images in Fig. 2a and Fig. 2b show the distinct micromorphologies of CdS and CN, respectively. Pristine CdS exhibits a granular morphology with particles loosely aggregated. In contrast, pure CN displays a flaky, layered structure, characteristic of graphitic materials, which often form stacked sheets or flaked layers. The composite material, CCN0.5, is depicted in Fig. 2c, where SEM analysis reveals that CdS nanoparticles are effectively coated with CN layers, resulting in a roughened surface texture. This modification in surface morphology suggests a strong interaction between CdS and CN, which is critical for enhancing the photocatalytic properties of the composite. An image of the high-resolution TEM (HR-TEM) image of CCN0.5 (Fig. 2d) depicts well-defined lattice fringes, indexed to the CdS (111) plane. The amorphous or graphitic-like structure of the carbon nitride (CN) component is characterized by diffuse and less defined features, typical for materials with disordered or layered structures [7]. Using energy-dispersive X-ray spectroscopy, the distribution of elements within CCN0.5 was analyzed (Fig. 2e-j). These maps display the spatial distribution of carbon and nitrogen, confirming the uniform presence of CN within the composite. The maps also reveal the distribution of sulfur (i) and cadmium (j), associated with the CdS component, validating the successful integration of CN and CdS within the composite structure [10,11].

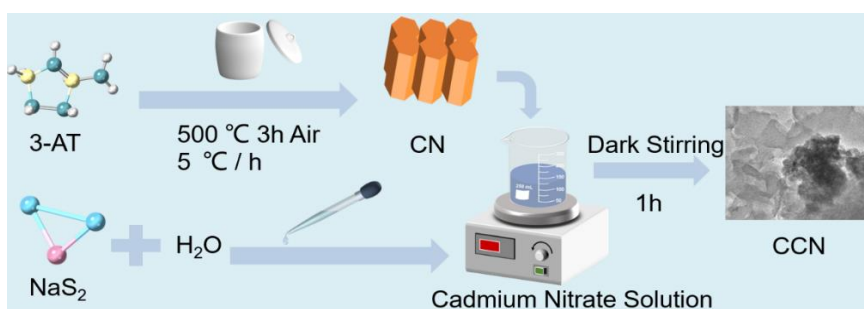


Fig. 1. Illustration of the preparation of CdS/C<sub>3</sub>N<sub>5</sub>.

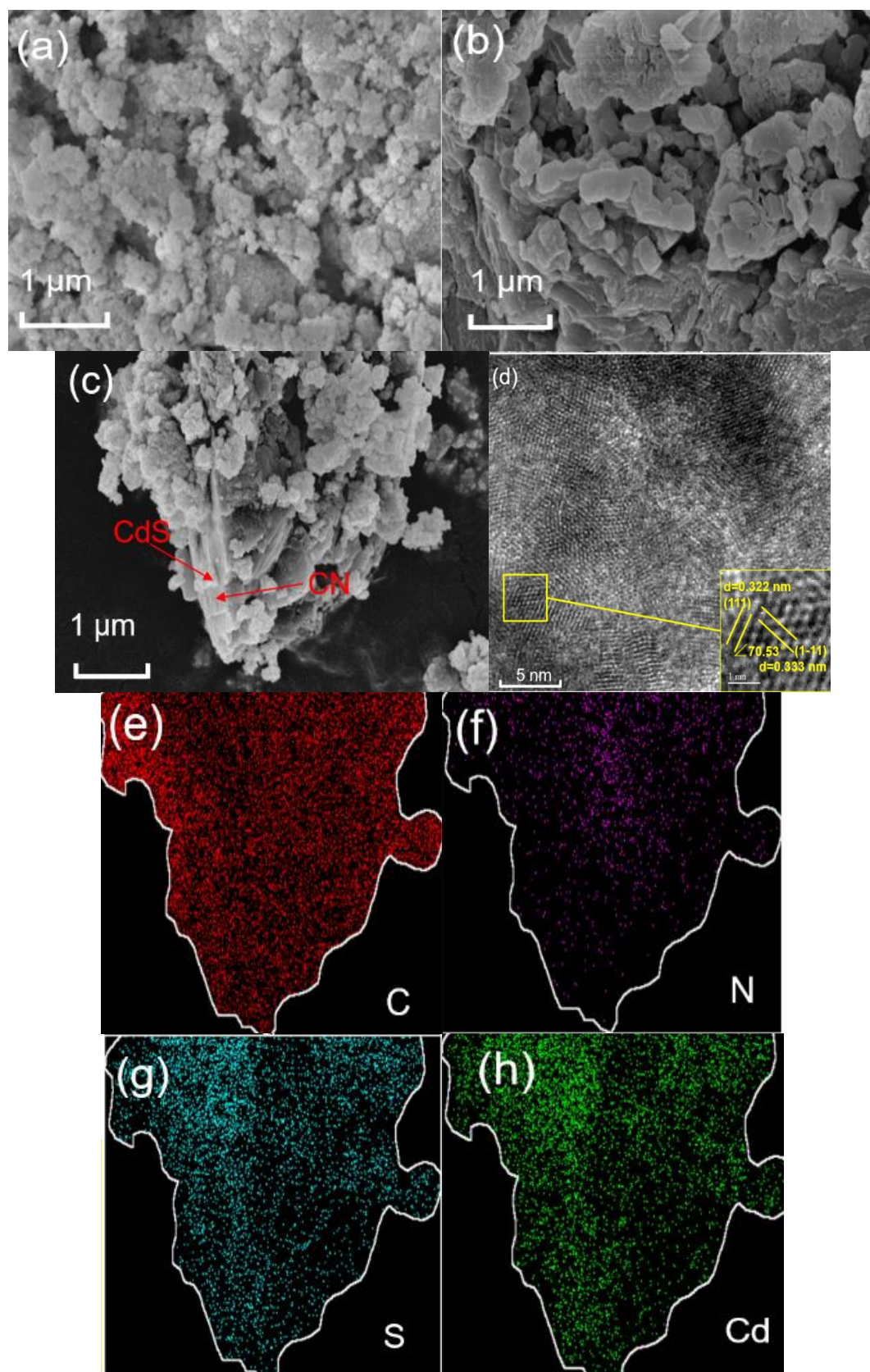


Fig. 2. SEM images of CdS (a), CN(b), CCN0.5(c). HR-TEM image (d), and EDS mapping images (e-h) of CCN0.5.

X-ray diffraction analysis was conducted on pure CdS, CN, and CCN composites to examine their crystalline structures (Fig. 3a). In the cubic zinc blende structure of CdS, the XRD patterns revealed significant peaks at  $26.5^\circ$  and  $43.9^\circ$ . The distribution of the element is mainly concentrated on the (111) and (220) crystal planes. This particular distribution pattern reflects the extremely high crystallinity of CdS samples, where the peak at  $26.5^\circ$  for the (111) plane represents the most densely packed layer, while the peak at  $43.9^\circ$  for the (220) plane reflects higher order reflections. In contrast, X-ray diffraction (XRD) analysis of pure graphitized carbon nitride (CN) shows a significant characteristic peak at approximately  $27^\circ$ , which corresponds to the (002) crystal face, suggesting a layered graphitic structure with lower crystallinity. This peak serves as a critical marker for identifying the CN component within the composites [12]. The XRD analysis of the CCN composites revealed additional peaks and shifts in peak positions compared to the pristine materials. Notably, a new peak emerged within the range of  $26.6$ - $27.2^\circ$  in the CCN samples. The results revealed that the heterostructure was successfully formed between CdS and CN, indicating that the synthesis of the composite has achieved the expected effect.

Raman spectrum is shown in Fig. 3b, The Infrared spectrum of CN has a peak at about  $1600\text{ cm}^{-1}$  which is usually thought to be from the C=C bond stretching vibration. The Raman peak at  $600\text{ cm}^{-1}$  for Cd-S is a typical one, which can be used to show the metal's stretching mode. In the composites, as the CN content increases from CCN0.125 to CCN2, the characteristics of CN become more pronounced in the spectra. This observation is consistent with data from scanning electron microscopy (SEM), which indicates that CdS particles dominate the surface morphology at lower CN concentrations.

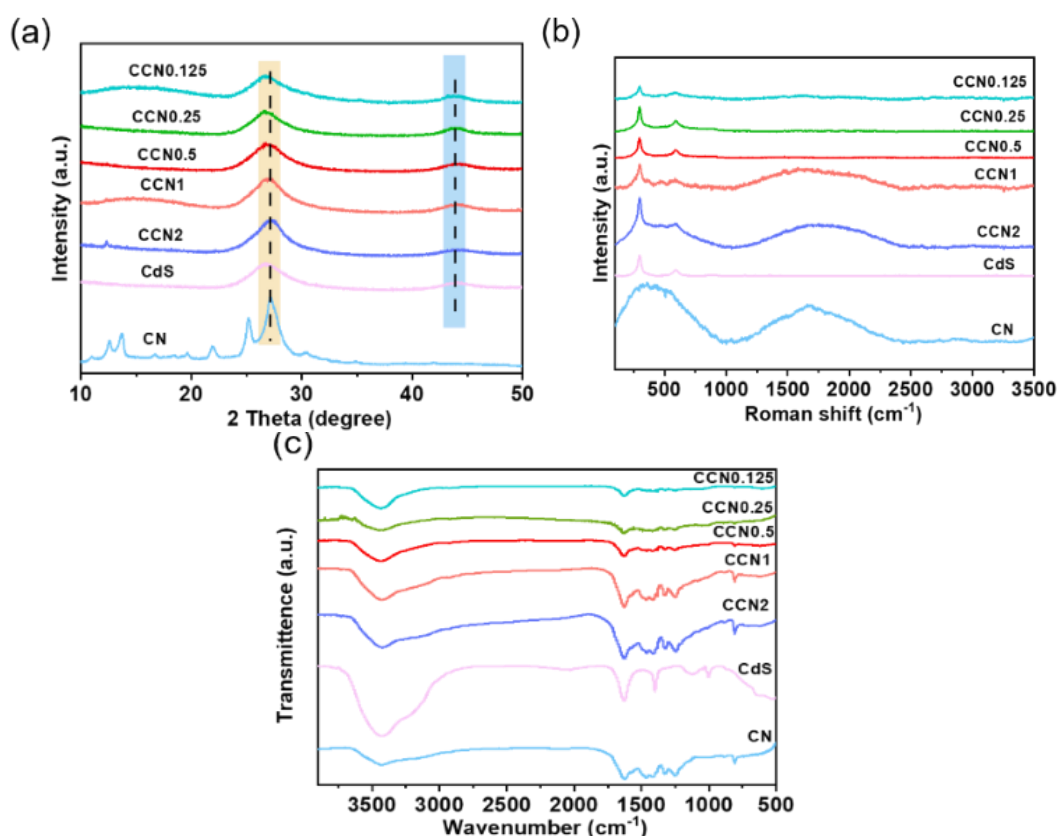


Fig. 3. (a) XRD patterns, (b) Raman, and (c) FT-IR spectra of as-prepared CdS, CN, CN/Cd.

FT-IR spectra were collected for C<sub>3</sub>N<sub>5</sub> and CdS composites to examine the chemical bonding and functional group composition within these materials. Fig. 3c shows that all compounds exhibit FT-IR patterns like C<sub>3</sub>N<sub>5</sub>, indicating that C<sub>3</sub>N<sub>5</sub> still retains its graphite structure. It is discovered that

the absorption peak of pure  $C_3N_5$  at  $3435\text{ cm}^{-1}$  mainly deals with the O-H bond which is a tensile vibration of water molecules, and the other peak at  $1624\text{ cm}^{-1}$  is H-O-H(vibration) bending occurs due to water's vibrations. The other peaks at  $1624$ ,  $1464$ , and  $1414\text{ cm}^{-1}$  are the vibrations of aromatic rings. Peaks at  $1324$  and  $1255\text{ cm}^{-1}$  are attributed to C-N stretching vibrations, and those at  $888$  and  $808\text{ cm}^{-1}$  are due to triazine ring breathing vibrations.

In the infrared spectrum of pure CdS samples, absorption peaks were identified, with a pronounced peak at  $3420\text{ cm}^{-1}$  attributed to the stretching vibration of the O-H bond. Additionally, a lesser peak at  $1620\text{ cm}^{-1}$  results from the bending vibration of H-O-H water molecules. Further, the peaks observed at  $1620$  and  $1400\text{ cm}^{-1}$  correspond to the antisymmetric and symmetric stretching vibrations of the carboxylic acid group ( $\text{COO}^-$ ), respectively. Impurities from the synthesis process are associated with peaks at  $1120$  and  $1001\text{ cm}^{-1}$ , while vibrations from Cd-S stretching are associated with peaks between  $700$  and  $500\text{ cm}^{-1}$ . For the composite sample, the peaks largely overlap those of the pure substances, with only minor shifts observed. The characteristic absorption peak of CdS appears at  $620\text{ cm}^{-1}$ , with weaker intensity in composites ranging from CCN0.125 to CCN0.5, likely due to the reduced addition of CdS, indicating predominantly physical interactions between the components. The absorption peaks at  $2923\text{ cm}^{-1}$  and  $2855\text{ cm}^{-1}$  are the signs of as well as symmetrical stretching vibrations of the methylene ( $-\text{CH}_2$ ) group, respectively [13-15]. The other absorption peaks are in most cases similar to those of the individual substances which make up the mixture. The physical interactions between the CN and CdS components are supported by the results from the Raman spectroscopy.

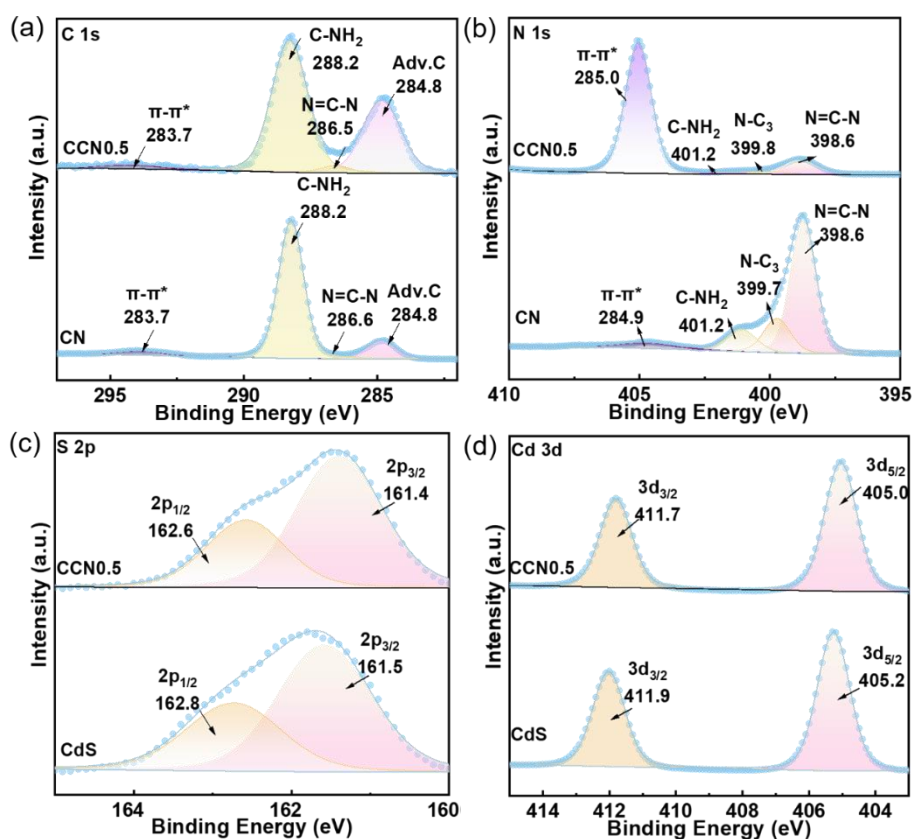


Fig. 4. C 1s (a), N 1s (b), S 2p (c), and Cd 3d (d) XPS spectra of CdS,  $C_3N_5$ , and CCN0.05.

The  $C_3N_5$ -based materials were thoroughly examined by elemental analysis and X-ray photoelectron spectroscopy (XPS). A peak at  $284.8\text{ eV}$ . The C 1s XPS spectrum of  $C_3N_5$  (Fig. 4a) shows the peaks at  $284.8\text{ eV}$ ,  $288.2\text{ eV}$ ,  $288.9\text{ eV}$ , and  $293.6\text{ eV}$  which are attributed to amorphous carbon (Adv. c), N=O-N structure, C-NH<sub>2</sub> groups and  $\pi$ - $\pi$  transitions. In the N 1s XPS high-resolution

spectrum of Fig. 4b, peaks of 398.6eV, 399.7eV, and 404.7eV indicate the C=N-C bond, N-C3 bond, and  $\pi$ - $\pi$  structure, respectively. In the case of pure CdS materials, as it is depicted in Fig. 4c, the doublet peaks are at 160.8eV and 162.0eV in the S2p spectrum are due to S 2p<sub>3/2</sub> and S 2p<sub>1/2</sub> separately. Moreover, Fig. 4d depicts the Cd 3d peaks at 404.7 eV and 411.4 eV, this marks the characteristic state of Cd<sup>2+</sup> in CdS. Significantly, a downward trend in the binding energy of S 2p and Cd 3d is observed in the CCN0.5 composites [16-19]. This shift of 0.2 eV in binding energy reflects a change in electron density, suggesting a potential electron transfer from CN to CdS. The upward shift in the binding energy of N 1s provides additional evidence for this charge transfer process.

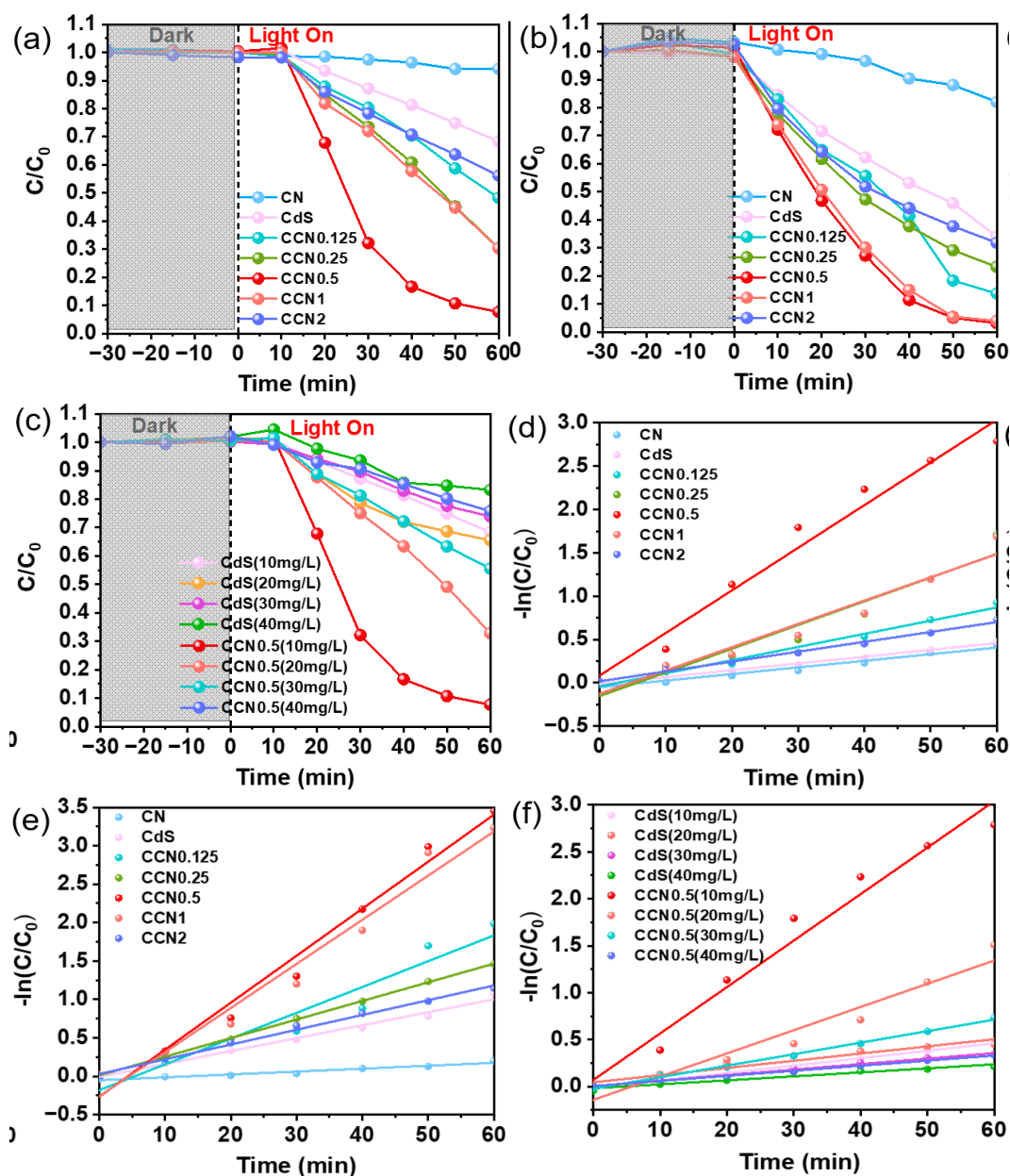


Fig. 5. (a) Degradation efficiency of MO and (b) RhB by samples under visible light irradiation. (c) Degradation efficiency of MO at varying concentrations. (d) Reaction kinetics for MO and (e) RhB in various reaction systems. (f) Reaction kinetics of CCN0.5 degrading MO at varying concentrations.

### 3.2. Photocatalytic performance

By evaluating the degradation effect of the composite on methylene orange (MO), the photocatalytic efficiency can be measured effectively. This method can intuitively reflect the material's ability to deal with organic pollutants under light conditions. MO (Fig. 5a) and rhodamine B (RhB) (Fig. 5b) solutions, each with a concentration of 10 mg/L. Without any catalyst and only under visible light, the photolysis of MO and RhB achieved degradation rates of merely 36% and 66%, respectively. Introducing 200 mg/L of the catalyst and a 30-minute dark stirring period to reach adsorption-desorption equilibrium resulted in minimal adsorption during the dark phase [20]. Under visible light irradiation, pollutant removal was primarily governed by the photodegradation process. The experiments demonstrated that with a CN to CdS mass ratio of 0.5 (CCN0.5), the removal rates peaked at 93.8% for MO and 96.8% for RhB. In comparison to the pure CdS, the degradation rate of MO in CCN was 57.8% higher. The necessity of the CN into CCN heterostructures to increase photocatalytic efficiency was stressed. Through the addition of CN, the elimination rate of Rhodamine B (RhB) was greatly enhanced, reaching 96.8%. The study found that the introduction of CN really boosted the photocatalytic process and improved the pollutant degradation ability of the material, as opposed to just 66% achieved by CdS alone. This indicates that the synergistic effect within the CCN heterostructure significantly boosts photocatalytic activity, particularly in degrading complex organic pollutants[21]. The observed trend suggests that the photocatalytic performance is optimal at a CN to CdS mass ratio of about 0.5 (CCN0.5), rather than increasing with higher CN content. The observed trend suggests that the photocatalytic performance is optimal at a CN to CdS mass ratio of about 0.5 (CCN0.5), rather than increasing with higher CN content. This phenomenon could be due to the optimal synergy formed at the CCN0.5 ratio, which maximizes the advantages of both components, while higher or lower CN contents might not be as conducive to maximizing photocatalytic performance. In Fig. 5c, the study also examined the impact of initial MO concentration. The degradation efficiency declined as the initial concentration of methylene orange was raised. This can be explained by the fact that the higher contaminant concentration saturates the surface of the available photocatalyst, thus decreasing its efficiency in carrying out the photocatalytic reaction. Higher concentrations of MO result in higher levels of intermediate products, which in turn somewhat inhibit the catalytic capability of CCN0.5.

$$\ln(C_0/C) = kt \quad (1)$$

The experimental data are in good accordance with the pseudo-first-order kinetic model as shown in Fig. 5d-f. The rate constant of the reaction is obtained from formula (1) where  $C_0$  and  $C_t$  are the concentration of methylene orange at the time the start time (0 min) and time  $t$  min. This fitting shows that the photocatalytic process follows the first-order kinetic reaction and can thus perfectly describe the degradation behavior of methylene orange during this process [22]. In the methylene orange degradation experiments (Fig. 5d), the CCN0.5 system achieved the highest  $k$  value at 0.04918 min<sup>-1</sup>. This value is 6.4 times greater than the C<sub>3</sub>N<sub>5</sub> system (0.00763 min<sup>-1</sup>), 6.3 times higher than the CdS system (0.00784 min<sup>-1</sup>), 3.2 times above the CCN0.125 system (0.01519 min<sup>-1</sup>), 1.8 times more than both the CCN0.25 system (0.02737 min<sup>-1</sup>) and the CCN1 system (0.02686 min<sup>-1</sup>), and 0.4 times greater than the CCN2 system (0.01138 min<sup>-1</sup>). Rhodamine B (RhB) degradation followed similar patterns, as shown in Fig. 5e. In Fig. 5f, during the degradation of a 10 mg/L methylene orange solution, the  $k$  value for the CCN0.5 system (0.049 min<sup>-1</sup>) was significantly higher than that of CdS (0.007 min<sup>-1</sup>). If the methylene orange concentration was multiplied by 20 mg/L, 30 mg/L, and 40 mg/L, then CCN0.5  $k$  values would have changed system were 0.02474 min<sup>-1</sup>, 0.01226 min<sup>-1</sup> and 0.00541 min<sup>-1</sup> were the ones that were significantly higher than those of CdS system, respectively. The latter are 0.00765 min<sup>-1</sup>, 0.00586 min<sup>-1</sup> and 0.00425 min<sup>-1</sup>, respectively. The findings revealed that the photocatalytic degradation efficiency of the CCN0.5 system was much more than that of the CdS system at higher concentrations. This result further confirms the advantages of CCN0.5 composites in improving photocatalytic performance, but the multiplicative factor decreased, aligning with the trend that higher concentrations result in reduced degradation rates. This indicates that while CCN0.5 significantly enhances photocatalytic activity, the efficiency decreases as the pollutant concentration increases, likely due to saturation effects and reduced light penetration.

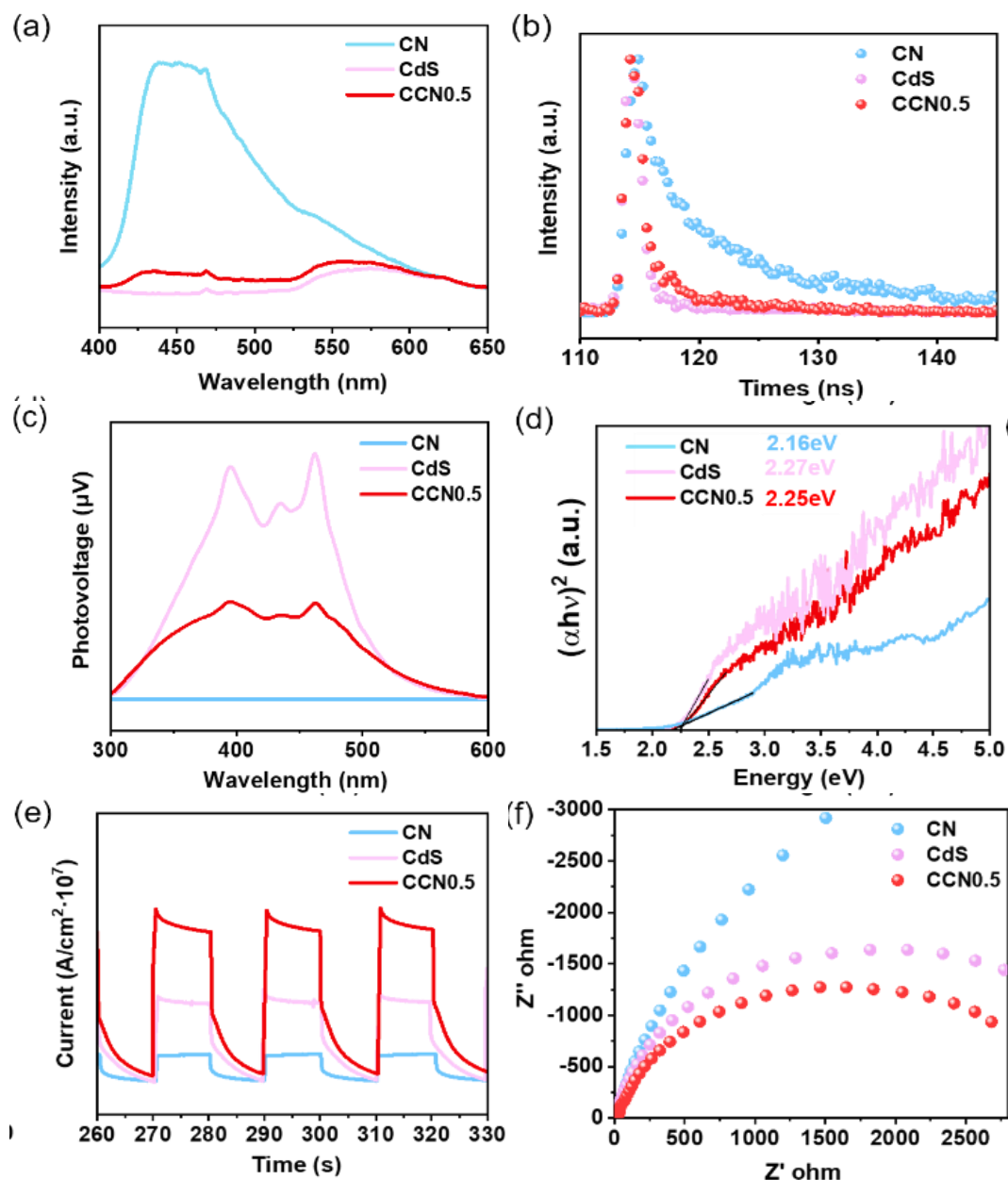


Fig. 6. (a) Steady-state PL spectra. (b) Time-resolved PL decay. (c) SPV. (d) UV-Vis diffuse reflectance spectra. (e) Photocurrent response and (f) EIS of g-C<sub>3</sub>N<sub>5</sub>, CdS, and CCN0.5.

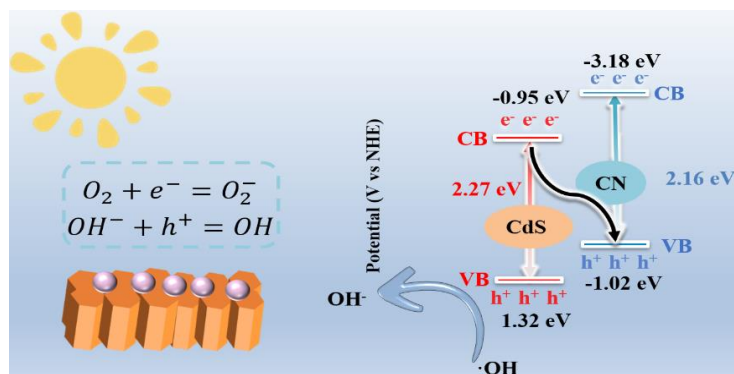


Fig. 7. Diagram illustrating the mechanism of CdS/C<sub>3</sub>N<sub>5</sub> system under visible light irradiation for photocatalytic degradation.

### 3.3. Enhanced photocatalytic performance mechanism

Photoluminescence (PL) analysis, as shown in Fig. 6a, The CN/CdS composites emission peak intensity is a significant parameter to measure the separation of photogenerated electron and hole. In this material, the intensity of the emission peak usually reflects the degree of recombination of electrons and hole pairs, which is slightly lower than that of CdS, highlighting CN's role in boosting charge separation efficiency. Significantly, the fluorescence intensity of CCN0.5 is much reduced compared to g-C<sub>3</sub>N<sub>5</sub>, indicating that CdS is effective in curbing the recombination of photogenerated carriers [23]. A time-resolved fluorescence decay spectrum obtained at the ns-level is shown in Fig. 6b, the fluorescence lifetime of CCN0.5 is shorter than that of pure CdS, pointing to swift electron transfer from CdS to CN at the interface. Additionally, the lifetime of fluorescence in CCN0.5, positioned between that of CdS and CN, confirms that the CdS/CN composite enhances electron conduction and facilitates the separation of photogenerated carriers.

Additionally, the Surface Photovoltage (SPV) spectroscopy (Fig. 6c) further elucidates the degree of charge separation and surface barriers of the excited states generated upon light absorption. Notably, Compared to the g-C<sub>3</sub>N<sub>5</sub> material, the CCN0.5 complex showed significantly enhanced surface photovoltage (SPV) response over the wavelength range of 300-600 nm, indicating accelerated photogenerated carrier separation efficiency. This observation aligns with the findings from electrochemical assays and photoluminescence (PL) studies, underscoring the superior degradation efficiency of CCN0.5. CN, CdS, and CCN0.5 direct band gaps were determined using *tauc* plots, which were found to be 2.16 eV (corresponding to 574 nm light), 2.27 eV (corresponding to 546 nm light), and 2.25 eV (corresponding to 551 nm light), respectively (Fig. 6d) [24-26].

Evaluating the photocatalytic activity of semiconductors relies heavily on their ability to transfer electrons. To further assess this, electrochemical assays were used to analyze the photoelectrochemical performance of the samples [27]. In the high-frequency region of the Nyquist plot, peaks are observed, indicative of processes constrained by electron transfer. Notably, the semicircle diameters in the plot for CCN0.5 are significantly reduced compared to those for g-C<sub>3</sub>N<sub>5</sub> and CdS (Fig. 6e) [28], suggesting enhanced electron transfer capabilities in CCN0.5 [20]. As is indicated in Fig. 6f, the electron separation efficiency of CCN0.5 surpasses that of both pure CdS and C<sub>3</sub>N<sub>5</sub>, as evidenced by its higher photocurrent density compared to these materials.

The fundamental energy bands in semiconductors consist of charged valence bands (VB) and hole-populated conduction bands (CB). A gap exists between these bands. Under light irradiation, in the photocatalysis process when the valence band electrons are photoexcited they will transition to the conduction band and at that moment, a hole is created in the valence band which forms an electron-hole pair (e<sup>-</sup>h<sup>+</sup>). Electrons in the conduction band possess strong reducing properties, whereas the holes exhibit strong oxidizing characteristics. Driven by an electric field, these electron-hole pairs disassociate and migrate towards the semiconductor's surface.

In the photocatalytic activity, the specific mechanism of charge separation and transport process at the interface of C<sub>3</sub>N<sub>5</sub> and CdS composites can be seen in the schematic diagram shown in Fig. 7. The VB potentials at 1.32 eV and -1.02 eV, respectively. Equation (2) governs the conduction band potential (CB):

$$E_g = E_{VB} - E_{CB} \quad (2)$$

where  $E_g$  denotes the specimen's band gap energy. Valence band and conduction band energies are represented by  $E_{VB}$  and  $E_{CB}$ , respectively [23]. It has been calculated that the CB potentials for CdS and g-C<sub>3</sub>N<sub>5</sub> are -0.95 eV and -3.18 eV, respectively.

The alignment of energy bands between C<sub>3</sub>N<sub>5</sub> and CdS forms an effective heterojunction structure, conducive to photocatalytic processes. Due to the conduction band potential of CdS being more negative than the O<sub>2</sub>/•O<sub>2</sub> redox potential (-0.33 eV vs. NHE), O<sub>2</sub> can be reduced by the photogenerated electrons in CdS to form superoxide radicals (•O<sub>2</sub>). On the other hand, the valence band potential of C<sub>3</sub>N<sub>5</sub> is more negative than the redox potential of •OH/H<sub>2</sub>O (2.4 eV vs. NHE), preventing the oxidation of water molecules into hydroxyl radicals by the photogenerated holes in C<sub>3</sub>N<sub>5</sub>. Consequently, a Z-scheme heterojunction photocatalytic system is suggested, where visible light (wavelengths above 425 nm) activates C<sub>3</sub>N<sub>5</sub> and CdS. This activation leads to the generation of photogenerated electrons (e<sup>-</sup>) in the CB of both materials and holes (h<sup>+</sup>) in their valence bands.

These charge carriers migrate along designated paths. Due to the more positive conduction band potential of CdS, electrons cannot accumulate in its conduction band. Therefore, electrons are transferred from the conduction band of CdS to the valence band of g-C<sub>3</sub>N<sub>4</sub>, where they combine with photogenerated holes. Consequently, the photogenerated electrons accumulate in the conduction band of g-C<sub>3</sub>N<sub>4</sub>, forming oxygen molecules (O<sub>2</sub>), while the remaining holes in CdS accumulate in its valence band, generating hydroxyl radicals (•OH).

These superoxide anions and holes participate in the reaction to form active oxygen species with strong oxidation, and effectively participate in the process of degrading harmful pollutants, oxidizing organic substrates, and producing decomposition products [29-30]. The photocatalytic process greatly boosts the charge separation because it optimizes the charge separation and migration processes, and at the same time reduces significantly the chance of recombination. Moreover, CdS exhibits less self-oxidation despite the presence of valence band holes. Therefore, the introduction of this heterogeneous structure not only enhances the activity of the composite in photocatalysis but also significantly improves its stability [20].

#### 4. Conclusions

In summary, this study achieved a successful synthesis of a composite material (CdS/CN) through a straightforward and efficient method. From a microscopic standpoint, it was evidenced that the formation of heterojunctions can effectively address inherent deficiencies within individual materials, and the composite material's degradation performance is greatly enhanced. Additionally, this study identified the optimal quality ratio for this enhancement.

#### Acknowledgments

The authors express their gratitude for the support provided by several institutions and funding bodies: the National Natural Science Foundation of China (Grant No. 22302079), the Natural Science Foundation of Jiangsu Province (Grant No. BK20230521), the Open Project Program of the State Key Laboratory of Photocatalysis on Energy and Environment at Fuzhou University (Grant No. SKLPEE-KF202306), and the Graduate Practical and Innovation Projects of Jiangsu Province (Grant No. SJCX23\_2096).

#### References

- [1] D. Monga, S. Basu, *J. Environ. Manage.* 336, 117570 (2023); <https://doi.org/10.1016/j.jenvman.2023.117570>
- [2] S.K. Lakhera, A. Rajan, R. T.P., N. Bernaudshaw, *Renew. Sustain. Energy Rev.* 152, 11694 (2021); <https://doi.org/10.1016/j.rser.2021.111694>
- [3] P. Rambabu, N.R. Peela, *Int. J. Hydrogen Energy* 48, 15406-15420 (2023); <https://doi.org/10.1016/j.ijhydene.2023.01.041>
- [4] J. Xu, P. Ye, Y. Cheng, Y. Wei, Y. Chen, *Energy Technol.*, 11, 2201452 (2023); <https://doi.org/10.1002/ente.202201452>
- [5] S.J. Shi, W. Wang, M. Teng, F. Kang, M. E'qi, Z. Huang, *J. Colloid Interface Sci.* 608, Part 1, 954-962 (2022); <https://doi.org/10.1016/j.jcis.2021.10.027>
- [6] C. Liu, J. Zhang, W. Wang, L. Chen, M. Zhu, *Surfaces Interfaces* 42, Part B, 103491 (2023); <https://doi.org/10.1016/j.surfin.2023.103491>
- [7] J. Xu, X. Zhang, W. Yan, T. Xie, Y. Chen, Y. Wei, *Inorg. Chem.* 63, 4279-4287 (2024); <https://doi.org/10.1021/acs.inorgchem.3c04408>
- [8] K. Bi, M. Wang, H. Li, *Surfaces Interfaces* 50, 10448 (2024); <https://doi.org/10.1016/j.surfin.2024.104487>

- [9] S.J. Lakshmi, C. Joel, R. B. Bennie, A.N. Paul Raj, Y. Anil Kumar, M. Shah Nawaz Khan, *J. Environ. Manage.* 360, 121086 (2024); <https://doi.org/10.1016/j.jenvman.2024.121086>
- [10] D. Monga, S. Basu, *J. Environ. Manage.* 336, 117570 (2023); <https://doi.org/10.1016/j.jenvman.2023.117570>
- [11] L.L. Wang, R.J. Sa, Y.C. Wei, X.F. Ma, C.G. Lu, H.W. Huang, E. Fron, M. Liu, W. Wang, S.P. Huang, J. Hofkens, M.B.J. Roefsaers, Y.J. Wang, J.H. Wang, J.L. Long, X.Z. Fu, R.S. Yuan, *Angew. Chem. Int. Ed.* 61, 4561 (2022); <https://doi.org/10.1002/anie.202204561>
- [12] J. Shi, W. Wang, M. Teng, F. Kang, M. E'qi, Z. Huang, *J. Colloid Interface Sci.* 608, 954-962 (2022); <https://doi.org/10.1016/j.jcis.2021.10.027>
- [13] B. Wang, H. Qiao, P. Guan, B. Yang, B. Liu, *Composite Interfaces* 30, 147-161 (2022); <https://doi.org/10.1080/09276440.2022.2076363>
- [14] X. Wang, K. Wu, W. Cao, K. Rui, W. Wang, R. Zhu, J. Zhu, Z. Yan, *Adv. Mater. Interfaces* 10, 5 (2022); <https://doi.org/10.1002/admi.202201627>
- [15] Z.R. Khan, M. Zulfequar, M. Shahid Khan, *J. Mater. Sci.* 46, 5412-5416 (2011); <http://doi.org/10.1007/s10853-011-5481-0>
- [16] X. Guan, M. Fawaz, R. Sarkar, C. Lin, Z. Li, Z. Lei, P.D. Nithinraj, P. Kumar, X. Zhang, J. Yang, *J. Mater. Chem. A* 11, 12837-12845 (2023); <https://doi.org/10.1039/d3ta00318c>
- [17] C. Fu, M. Zhao, X. Chen, G. Sun, C. Wang, Q. Song, *Appl. Catal. B Environ.* 332, 122752 (2023); <https://doi.org/10.1016/j.apcatb.2023.122752>
- [18] C. Fu, T. Wu, G. Sun, G. Yin, C. Wang, G. Ran, Q. Song, *Appl. Catal. B Environ.* 323, 122196 (2023); <https://doi.org/10.1016/j.apcatb.2022.122196>
- [19] J. Zhang, B. Jing, Z. Tang, Z. Ao, D. Xia, M. Zhu, S. Wang, *Appl. Catal. B Environ.* 289, 120023 (2021); <https://doi.org/10.1016/j.apcatb.2021.120023>
- [20] Y. Cui, *J. Catal.* 36, 372-379 (2015); [https://doi.org/10.1016/S1872-2067\(14\)60237-0](https://doi.org/10.1016/S1872-2067(14)60237-0)
- [21] M. Liu, P. Ye, M. Wang, L. Wang, C. Wu, J. Xu, Y. Chen, *J. Environ. Chem. Eng.* 10, 108436 (2022); <https://doi.org/10.1016/j.jece.2022.108436>
- [22] W. Liao, Z. Yang, Y. Wang, S. Li, C. Wang, Z. Zhou, *Small* 478, 147346 (2023); <https://doi.org/10.1016/j.jcej.2023.147346>
- [23] S. Bellamkonda, G. Ranga Rao, *Catal. Today* 321-322, 18-25 (2019); <https://doi.org/10.1016/j.cattod.2018.03.025>
- [24] H. Yu, R. Shi, Y. Zhao, T. Bian, Y. Zhao, C. Zhou, G.I.N. Waterhouse, L.-Z. Wu, C.-H. Tung, T. Zhang, *Adv. Mater.* 29, 1605148 (2017); <https://doi.org/10.1002/adma.201605148>
- [25] L.L. Wang, Y. Hu, J.H. Xu, Z.F. Huang, H.X. Lao, X.W. Xu, J. Xu, H. Tang, R.S. Yuan, Z. Wang, Q.Q. Liu, *Int. J. Hydrogen Energy* 48, 16987 (2023); <https://doi.org/10.1016/j.ijhydene.2023.01.172>
- [26] L.L. Wang, T. Yang, L.J. Peng, Q.Q. Zhang, X.L. She, H. Tang, Q.Q. Liu, *Chinese J. Catal.* 43, 2720 (2022); [https://doi.org/10.1016/S1872-2067\(22\)64133-0](https://doi.org/10.1016/S1872-2067(22)64133-0)
- [27] J. Luo, H. Han, X. Wang, X. Qiu, B. Liu, Y. Lai, X. Chen, R. Zhong, L. Wang, C. Wang, *Nature Mater.* 328, 122495 (2023); <https://doi.org/10.1016/j.apcatb.2023.122495>
- [28] L. Wang, G. Tang, S. Liu, H. Dong, Q. Liu, J. Sun, H. Tang, *Chem. Eng. J.* 428, 131338 (2022); <https://doi.org/10.1016/j.jcej.2021.131338>
- [29] S.Y. Luo, S.P. Li, S. Zhang, et al., *Sci. Total Environ.* 806, 150622 (2022); <https://doi.org/10.1016/j.scitotenv.2021.150662>
- [30] W. Yan, Y. Xu, S. Hao, Z. He, L. Wang, Q. Wei, J. Xu, H. Tang, *Inorg. Chem.* 61, 4725-4734 (2022); <https://doi.org/10.1021/acs.inorgchem.2c00045>